Research Article

ADVANCED PHOTONICS

On-chip optical vector analysis based on thin-film lithium niobate single-sideband modulators

Hanke Feng,[a] Tong Ge,[a] Yaowen Hu,[b,c] Zhenzheng Wang,[a] Yiwen Zhang,[a] Zhaoxi Chen,[a] Ke Zhang,[a] Wenzhao Sun,[a,d,e] and Cheng Wang[a,*]

[a]City University of Hong Kong, Department of Electrical Engineering and State Key Laboratory of Terahertz and Millimeter Waves, Kowloon, Hong Kong, China
[b]Peking University, State Key Laboratory for Mesoscopic Physics and Frontiers Science Center for Nano-Optoelectronics, School of Physics, Beijing, China
[c]Harvard University, John A. Paulson School of Engineering and Applied Sciences, Cambridge, Massachusetts, United States
[d]City University of Hong Kong (Dongguan), Dongguan, China
[e]City University of Hong Kong Shenzhen Research Institute, Center of Information and Communication Technology, Shenzhen, China

Abstract. Optical vector analysis (OVA) is an enabling technology for comprehensively characterizing both amplitude and phase responses of optical devices or systems. Conventional OVA technologies are mostly based on discrete optoelectronic components, leading to unsatisfactory system sizes, complexity, and stability. They also encounter challenges in revealing the on-chip characteristics of integrated photonic devices, which are often overwhelmed by the substantial coupling loss and extra spectral response at chip facets. In this work, we demonstrate a miniaturized OVA system based on broadband single-sideband (SSB) modulators on a thin-film lithium niobate (LN) platform. The OVA could provide a direct probe of both amplitude and phase responses of photonic devices with kilohertz-level resolution and tens of terahertz of measurement bandwidth. We perform *in situ* characterizations of single and coupled microring resonators fabricated on the same chip as the OVA, unfolding their intrinsic loss and coupling states unambiguously. Furthermore, we achieve the direct measurement of collective phase dynamics and density of states of the Bloch modes in a synthetic frequency crystal by *in situ* OVA of a dynamically modulated microring resonator. Our OVA system provides a compact, high-precision, and broadband solution for characterizing future integrated photonic devices and circuits, with potential applications ranging from optical communications, biosensing, and neuromorphic computing, to quantum information processing.

Keywords: optical vector analysis; thin film lithium niobate; integrated microwave photonics.

Received Apr. 28, 2024; revised manuscript received Sep. 10, 2024; accepted for publication Oct. 18, 2024; published online Dec. 10, 2024.

[DOI: 10.1117/1.AP.6.6.066006]

1 Introduction

Accurately revealing the spectral information of optical devices and systems is of the utmost importance for comprehending performance characteristics, understanding the underlying physics, and discovering potential applications.[1] Optical vector analysis (OVA), analogous to electrical vector analysis, is a powerful tool to perform such characterizations by capturing both amplitude and phase information.[2–16] Traditional OVA approaches primarily rely on optical interferometry[2] or optical channel estimation techniques.[3,4] The necessity of laser wavelength scanning in these methods often leads to inadequate measurement resolutions on the megahertz level, posing challenges in keeping pace with the fine spectral features in emerging optical devices (down to the kilohertz level). Recently, OVAs based on the concept of microwave photonics (MWP)[17,18] have been proposed and demonstrated[5–15] by performing optical frequency scanning and signal measurement in the electrical domain through

*Address all correspondence to Cheng Wang, cwang257@cityu.edu.hk

electro-optic (EO) modulation and photodetection. Benefiting from the ultrahigh resolution frequency sweeping and accurate vector measurement ability in the electrical domain, MWP-based OVA technology is endowed with hyperfine resolution down to the theoretically hertz level and the capability to extract both amplitude and phase information.[8] Nevertheless, all existing MWP-based OVA systems have been demonstrated using either all-discrete optical devices[5–13] or by combining silicon signal processing chips with traditional off-the-shelf modulators.[14,15] These approaches inevitably lead to increased system cost, bulkiness, and complexity, prohibiting the deployment in scenarios involving mobile and remote devices, such as drones, autopilot vehicles, and satellites. In addition, all aforementioned demonstrations are *ex situ* measurements, where the test equipment and devices under test (DUTs) are physically separated, which is prone to environmental fluctuations and de-embedding errors from the link components between the test instrument and DUTs. This is particularly problematic for measuring the spectral responses of on-chip photonic devices, which are often overwhelmed by substantial fiber–chip coupling losses. Moreover, the presence of undesired Fabry–Perot interference caused by coupling facet reflection often introduces additional undesired amplitude and phase features, resulting in substantial uncertainties in the measurement results.

The recently emerged thin-film lithium niobate (LN) MWP platform[19] exhibits tremendous potential for resolving the aforementioned challenges and realizing integrated OVA systems with dramatically reduced size, weight, and power consumption (SWaP), owing to its unique EO properties and low optical loss characteristics.[20,21] To date, many key MWP building blocks have been demonstrated on the LN platform, including linear and broadband EO modulators,[22–26] low-loss functional elements with various spectral responses,[27–30] EO/Kerr comb sources,[31,32] and on-chip stimulated Brillouin scattering (SBS) devices.[33,34] The excellent performances demonstrated in these building blocks could significantly enhance the MWP system metrics, including bandwidth, noise figure, reconfigurability, and spectral resolution.[17] Endeavors to further integrate these elements into chip-scale systems have led to integrated LN MWP systems with unparalleled performance, including ultrahigh speed, low-power analog signal processors,[19] and broadband multifunction photonic millimeter-wave radars.[35]

Here, we demonstrate an integrated OVA system based on an LN photonic integrated circuit capable of directly probing the amplitude and phase responses of various optical devices. The integrated OVA system builds on an SSB modulator, which consists of a broadband phase modulator and a reconfigurable flat-top filter, for high-fidelity EO conversion. Fabricated from a 4-in. wafer-scale process, the device is capable of sweeping the modulated optical probe signal with a 20-dB sideband suppression ratio (SSR) and 50-kHz frequency resolution. The total measurement bandwidth could be extended up to tens of terahertz by shifting and stitching different measurement channels. We further leverage the excellent scalability of the LN platform to demonstrate *in situ* OVA by integrating various photonic DUTs with the SSB modulators on the same chip, enabling unambiguous characterization of the coupling states and lifetimes of single and coupled microring resonators with suppressed background Fabry–Perot fringes. Further performing *in situ* OVA of an actively modulated microresonator enables, for the first time, direct probing of the collective phase dynamics of the Bloch modes in a synthetic frequency crystal.

2 Results

2.1 Integrated Single-Sideband Modulators

Figure 1 shows the schematic illustration and working principle of our proposed OVA system. A continuous-wave optical carrier [f_c, (i)] is modulated by high-resolution scanning RF probe signals [f_1–f_2, (ii)] using an on-chip EO phase modulator, which generates typical double-sideband (DSB) signals with scanning optical frequencies in both sidebands (iii). The DSB signals are subsequently reshaped by an optical flat-top bandpass filter [blue curve in (iv)] that preserves only the carrier and one sideband, leading to SSB modulation (iv). Afterward, the scanning SSB signals capture the frequency-dependent amplitude and phase response of the DUTs and mix with the optical carrier at the photodetector, rendering high-resolution electrical signals that preserve both amplitude and phase information of the different DUTs (vi) thanks to the coherent nature of the entire process (more details on the OVA theories can be found in Appendix C). Apart from directly using this SSB modulator as a miniaturized OVA instrument in a similar manner to that in earlier reports,[5–13] our integrated OVA system also enables *in situ* measurement by integrating various on-chip DUTs next to the SSB modulators. In the *in situ* measurement mode, the remaining SSB signals are divided into two branches, wherein one is directed toward the on-chip DUT [using double microring resonators as an example, (v)], and the other goes through a bare optical waveguide with the same path length as a reference arm for calibrating the OVA system. The amplitude and phase response of on-chip DUTs will be obtained through the same process as described above.

The integrated LN OVA is fabricated on a 4-in. wafer-scale manufacturing platform using an ultraviolet (UV) stepper lithography system (more details are provided in Appendix A). Figure 2(a) shows the false-color optical image of the LN SSB modulator, consisting of a high-performance phase modulator (EO bandwidth >50 GHz, $V_\pi \sim 6$ V) with advanced slotted-electrodes[26] and a tunable flat-top optical filter based on a ring-assisted Mach–Zehnder interferometer (RAMZI) configuration.[36–38] The left inset in Fig. 2(a) shows a photograph of a fabricated chip clamped by tweezers. Middle and right insets highlight details of the slotted electrodes and thermo-optic (TO) phase shifter through scanning electron microscope (SEM) images. The operation principle of the RAMZI flat-top filter is shown in Fig. 2(b), where the top and middle panels plot the optical transmission and phase response, respectively, of a microring resonator (light blue) and a Mach–Zehnder interferometer (MZI, dark blue), as functions of wavelength detuning [normalized by the free spectral range (FSR) of MZI]. To build a flat-top bandpass filter,[37] the FSR of the microring resonator should equal half the FSR of the MZI, such that the extra phase induced by microring resonances always applies on the slope (i.e., quadrature point) of the sinusoidal transfer function of the MZI. By carefully engineering the coupling coefficient between the microring resonator and the bus waveguide to be $\kappa = 0.94$ using a multimode interferometer (MMI), an ideal phase relationship between the microring and the MZI could be achieved, leading to a sharp transition from on to off states (or vice versa) near the quadrature points (more details are provided in Appendix B). As a result, the transmission spectrum is strongly modified from the typical sinusoidal curve of an asymmetric MZI to a "box-like" response with near-flat and

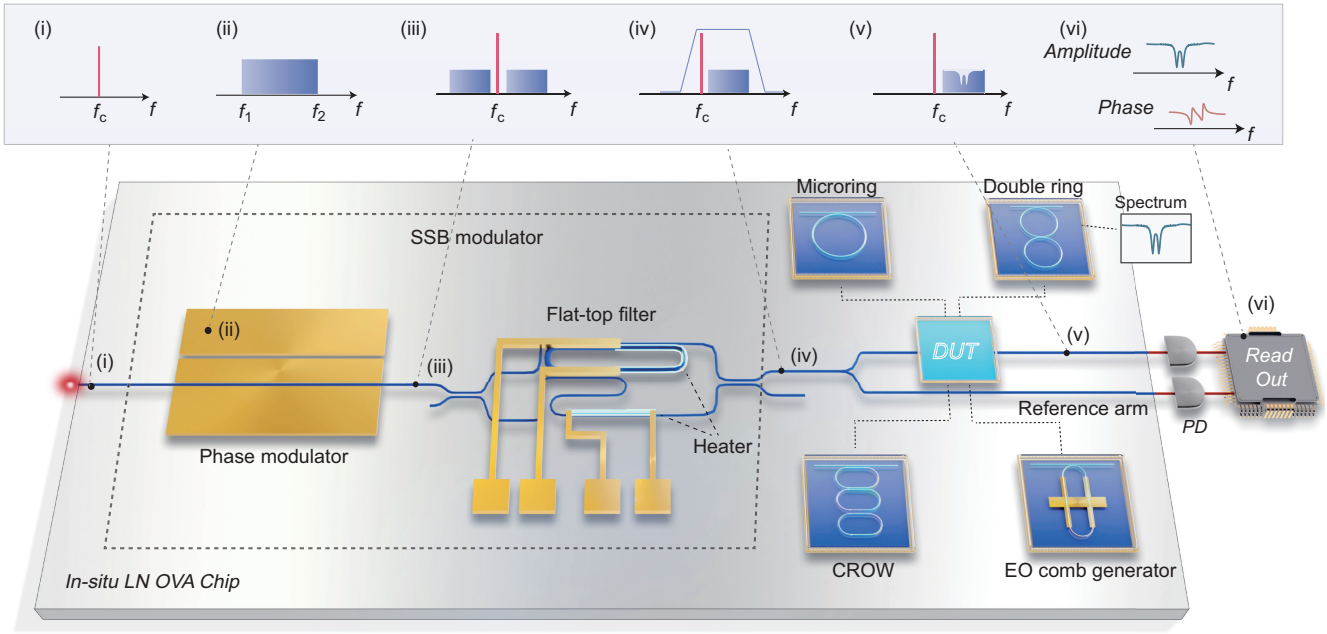

Fig. 1 Schematic illustration and working principle of the integrated LN OVA system. The SSB modulator consists of a phase modulator for signal upconversion and a tunable flat-top bandpass filter for SSB suppression. Various passive and active DUTs are fabricated on the same chip as the SSB modulator for *in situ* measurements. Insets (i)–(vi) schematically illustrate the spectra of optical and electrical signals at different locations of the chip.

periodically occurring pass- and stopbands [bottom panel of Fig. 2(b)]. In actual experiments, non-ideal coupling coefficients κ could lead to an undesirable phase relationship at the off-resonance points [dashed lines in top panel of Fig. 2(c)], resulting in ripples in the pass/stopbands [bottom panel of Fig. 2(c)] and compromised extinction ratios.

To take full advantage of the broad modulation bandwidths of LN modulators, we design FSRs of the microring resonator and the asymmetric MZI to be 120 and 60 GHz, respectively, resulting in a flat passband of ~50 GHz. The resonant wavelength of the microring resonator is aligned to the quadrature point of the MZI by TO phase shifters fabricated in the vicinity of both the microring resonator and one arm of the MZI [Fig. 2(a)]. The measured spectral response of the RAMZI filter in a representative channel is shown in Fig. 2(d) (gray), with a 210 dB/nm roll-off slope and a 20-dB extinction ratio. By locating the optical carrier at the edge of the pass band, SSB modulation could be achieved within a wide RF frequency range between 10 and 50 GHz, with measured optical SSR consistently at ~20 dB [Fig. 2(d)]. Moreover, the passband of our RAMZI filter could be flexibly shifted without affecting the flat-top nature by simultaneously tuning the TO phase shifters on the microring and the MZI. Figure 2(e) shows a series of measured flat-top bandpass profiles when the TO phase shifters are adjusted to set the relative phases of MZI at 0, $\pi/2$, π, and $3\pi/2$ (from top to bottom), with TO tuning efficiencies of 12 pm/mW for the microring resonator and 5 pm/mW for the MZI, respectively. The ability to shift the passband over a full period unlocks the possibility of achieving an ultrawide measurement bandwidth by separately performing OVA within individual bands and subsequently shifting and stitching the channels.

2.2 In Situ OVA of Integrated Passive Devices

To implement the *in situ* measurement of integrated photonic devices, we fabricate various DUTs next to the SSB modulators on the same LN chip and perform OVA using the experimental setup shown in Fig. 3(a). High-resolution sweeping RF signals (10 to 50 GHz) from an electrical vector network analyzer (EVNA) are used to drive the SSB modulator and probe the optical properties of DUT following the working principle introduced above. The signals are converted back into the electrical domain using a high-speed photodetector and analyzed at the other port of the EVNA (more details are provided in Appendix D). We use RF power of 5 dBm to avoid the impact from higher-order sidebands and noise, staying in the small-signal modulation regime (more details are provided in Appendix G).[13] The fabricated passive on-chip devices for the *in situ* OVA include a single-ring resonator, a double-ring coupled-resonator system, and coupled-resonator optical waveguides (CROWs). These devices are fundamental building blocks for a variety of applications in integrated photonics, such as electromagnetically induced transparency (EIT) models,[39] non-Hermitian photonics,[40] and optical filters.[41]

Figure 3(b) depicts the measured and fitted amplitude and phase responses of a single microring resonator, showing two optical modes (a fundamental and a high-order mode) simultaneously present in the measurement window with resonant frequencies separated by 6.2 GHz. The amplitude responses of the two resonances indicate notch depths of 4 and 11 dB, and full width at half-maximum linewidths (in linear scale) of 500 and 378 MHz, respectively. The measured amplitude responses are in good agreement with those obtained using the traditional laser scanning method (yellow dashed lines), but with substantially suppressed background Fabry–Perot fringes thanks to the

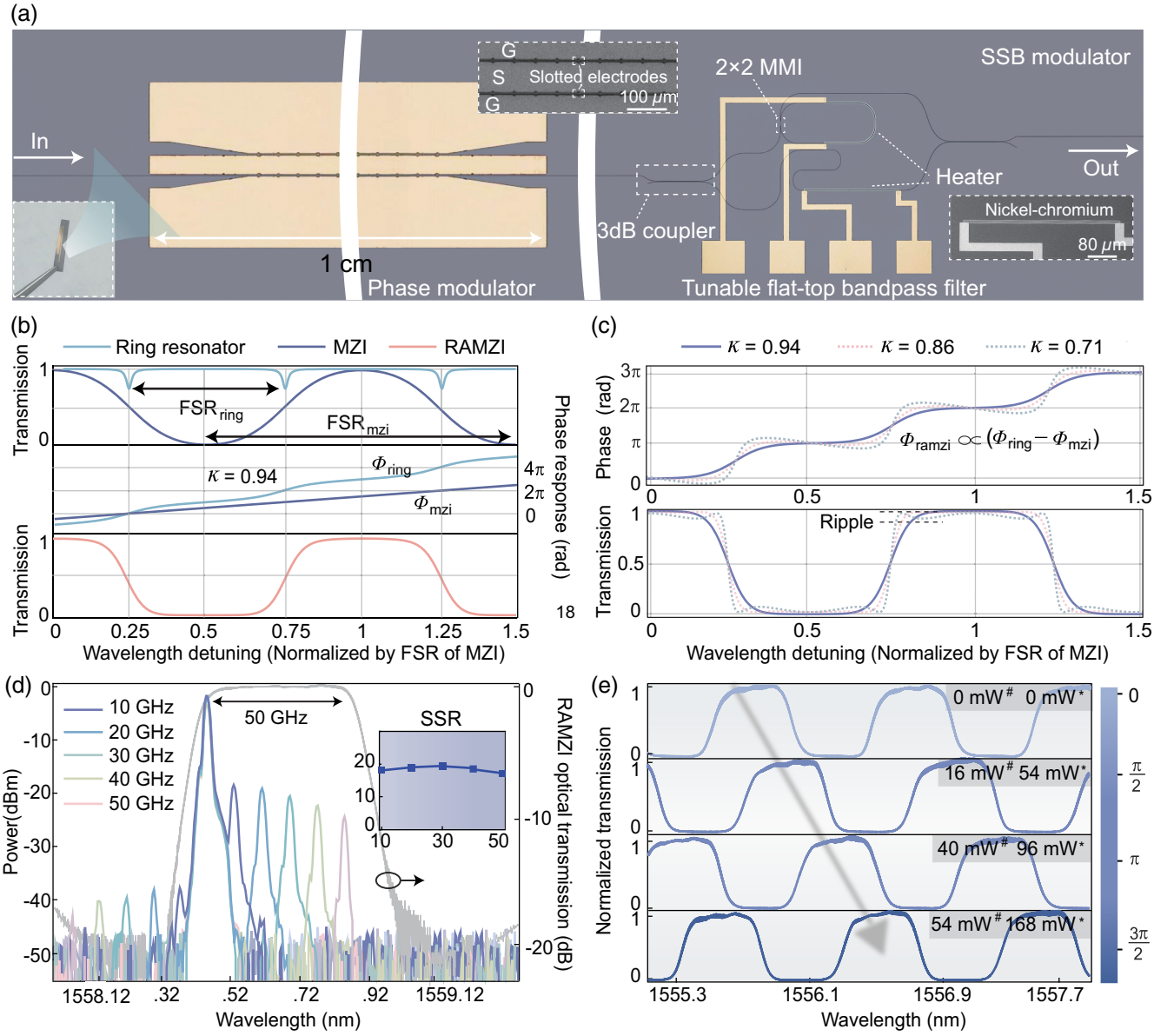

Fig. 2 Principle and characteristics of LN SSB modulators. (a) Optical image (false-color) of the LN SSB modulator, including a phase modulator and an RAMZI tunable flat-top filter. Left inset: photograph of the chip clamped by tweezers. Middle and right insets: scanning electron micrographs (SEMs) of the slotted modulation electrodes and the TO phase shifter, respectively. (b) Principle of the RAMZI flat-top filter. Top and middle panels show the output optical amplitude transmission and phase response, respectively, of a microring resonator (light blue) and an unbalanced MZI (dark blue), as functions of normalized wavelength detuning (per FSR of MZI). By aligning the resonance notches to the quadrature points of the MZI and choosing a proper coupling state ($\kappa = 0.94$), the additional phase shift from the microring resonator modifies the linear phase response of MZI, turning the full RAMZI transfer function to a "box-like" flat-top bandpass profile, as shown in the bottom panel. (c) Simulated phase response and output transmission of the RAMZI filter at different coupling states of the microring resonator, showing undesired ripples in the pass/stopbands in the cases of nonideal coupling coefficients. (d) Measured optical transmission spectrum of the RAMZI filter (gray) with a 50 GHz flat-top passband, a 210 dB/nm roll-off slope, and a 20-dB extinction ratio, enabling SSB modulation (color-coded output spectra) with 20-dB SSR within 10 to 50 GHz (inset). (e) Measured bandpass profiles when the relative phases of MZI are set at 0, $\pi/2$, π, and $3\pi/2$ (from top to bottom). #Heater power of ring resonator. *Heater power of MZI.

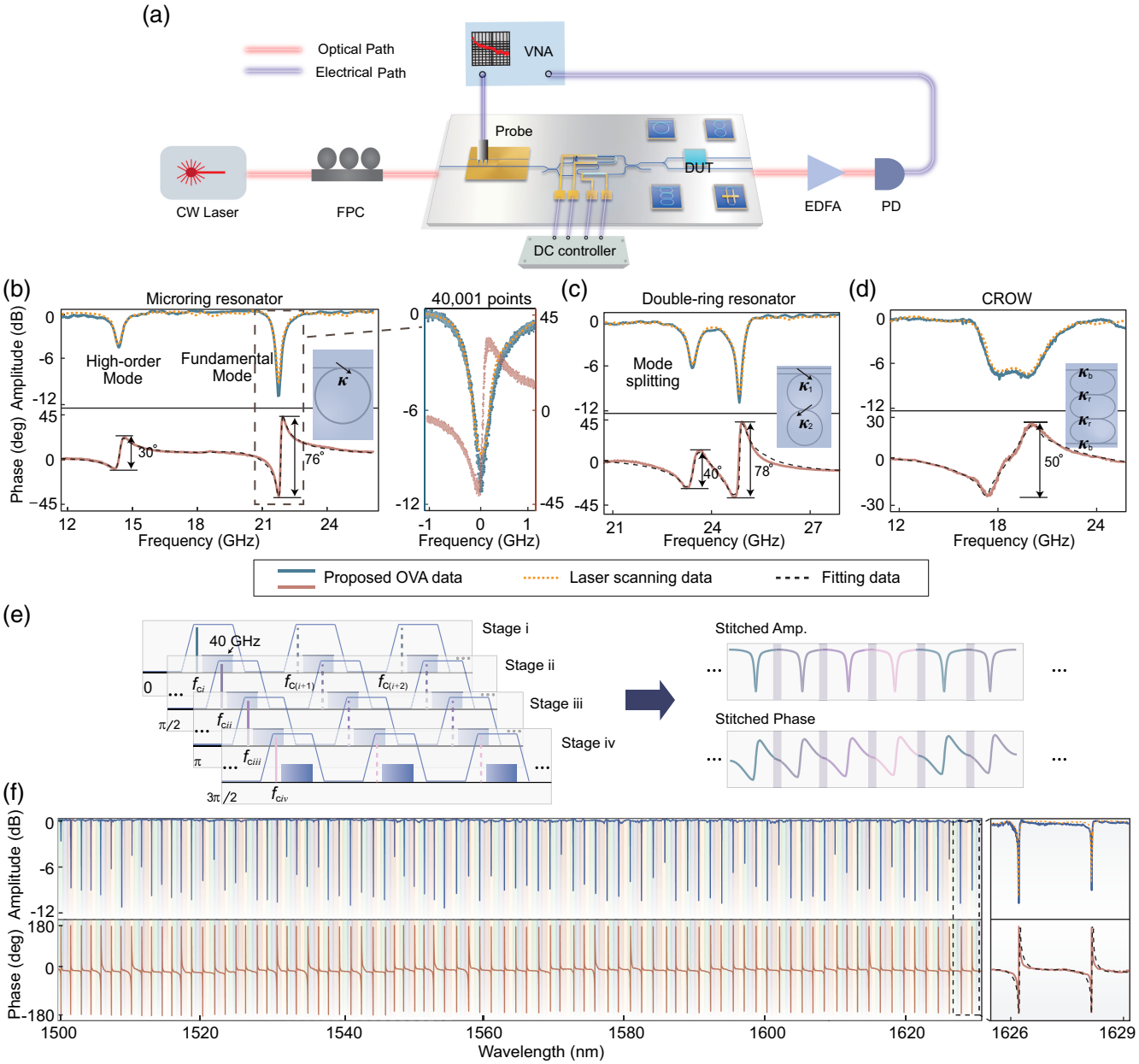

Fig. 3 *In situ* OVA for on-chip passive devices. (a) Experimental setup for an *in situ* OVA system based on integrated SSB modulation. CW, continuous-wave; FPC, fiber polarization coupler; DUT, device under test; EDFA, erbium-doped fiber amplifier; PD, photodetector. (b)–(d) Measured amplitude (blue) and phase (red) responses using OVA, together with laser scanning data (yellow dashed) of a single ring resonator (b), a double ring system (c), and a CROW (d). Black dashed lines correspond to fitted phase responses. Right side of panel (b) shows fine measurement results around one resonance dip, with 40,001 data points and a resolution of 50 kHz. (e) Working principle of a seamless stitching process for broad measurement bandwidth by tuning the position of the bandpass filter and optical carrier. (f) Ultrabroadband OVA from 1500 to 1630 nm for a single microring resonator. Inset at far right shows the zoom-in view of the measured responses between 1626 and 1629 nm, indicating an overcoupling state.

in situ measurement mode (see Note II in the Supplemental Material). Importantly, the vector analysis adopted in our experiments allows us to directly probe the phase responses of these resonances and infer their coupling states (under/critical/over), which is typically not possible in an amplitude-only transmission spectrum measurement. In this particular case, we measure resonant phase jumps of 30 deg and 76 deg for the two resonances, both of which correspond to undercoupling states. Further fitting the experimental results with the theoretical model (dashed black curves) provides unambiguous and quantitative analysis on the coupling coefficients of these two modes at $\kappa_1 = 0.092$ (high-order mode) and $\kappa_2 = 0.093$ (fundamental mode);

as well as the intrinsic quality factors of 3.86×10^5 and 9.03×10^5, respectively. To validate the high resolution of our OVA system, the right panel of Fig. 3(b) shows the fine measurement results near one resonance notch, which comprises 40,001 data points over a span of 2 GHz, resulting in a resolution of 50 kHz, currently limited by the linewidth of our tunable laser. The implementation of a narrow linewidth laser could in principle enable hyperfine resolution down to the hertz-level.[8,13]

For more complicated photonic systems, such as the double-ring resonator shown in Fig. 3(c), our *in situ* OVA system could also reliably capture the resonant phase jumps for both split modes, i.e., 40 deg and 78 deg in this case. The fitting results reveal an initial resonance frequency difference (Δf) of 0.457 GHz between the two ring resonators due to fabrication nonuniformity, a ring-bus coupling coefficient of $\kappa_1 = 0.16$, and a coupling coefficient between the two ring resonators of $\kappa_2 = 0.03$. We further conduct an *in situ* vector analysis of a triple-ring CROW system at the through port, as shown in Fig. 3(d). Assuming the two ring–ring couplers (κ_r) and the two ring-bus couplers (κ_b) are identical, our measurement and fitting results again lead to reliable estimation of the coupling coefficients, i.e., $\kappa_r = 0.26$ and $\kappa_b = 0.03$. Such information could be highly valuable in inferring the actual operating states of complex photonic systems and providing instruction for achieving the design targets. For example, if the objective is to design a Butterworth filter, we could straightforwardly conclude that both coupling coefficients need to be slightly increased (ideally: $\kappa_r = 0.33$ and $\kappa_b = 0.04$).

Building upon the broadband reconfigurability of our flat-top filter, we demonstrate ultrawide measurement bandwidth up to tens of terahertz by stitching a series of 40-GHz measurement channels, as the schematic diagrams in Fig. 3(e) illustrate. Within each 120-GHz spectral period of the flat-top filter, e.g., between f_{ci} and $f_{c(i+1)}$, we strategically perform four measurements by biasing the filter at relative MZI phases of 0, $\pi/2$, π, and $3\pi/2$, leading to a frequency offset of 30 GHz between adjacent measurement channels. Considering each measurement could yield a reliable measurement bandwidth of 40 GHz (between $f_c + 10$ GHz and $f_c + 50$ GHz) with a near-flat spectral response and high SSR; this provides an effective overlapping region of 10 GHz between adjacent channels that could be used to stitch amplitude and phase information of the DUT over a wide frequency range (see Note III in the Supplemental Material). Figure 3(f) shows the measured spectral responses of a single microring resonator from 1500 to 1630 nm (16.2 THz), exhibiting a total of 84 resonance notches with an FSR of 219 GHz. The inset shows a zoom-in view between 1626 and 1629 nm with two adjacent resonance notches of the same optical mode. Through an analysis similar to the above, we conclude this resonator is at an overcoupling state with a coupling coefficient of 0.11. It should be noted that currently the absolute frequencies of measurement channels are not accurately referenced, since they are only stitched together numerically. Further calibrating the optical carriers in each channel using a phase-stable fiber cavity or interferometer could enable applications that require broadband absolute wavelength accuracy, such as extraction of high-order dispersion information.[16]

2.3 In Situ OVA of Integrated Active Devices

We further demonstrate that our integrated OVA system facilitates the direct characterization of both amplitude and phase evolutions of an actively modulated microring resonator, providing additional probing degrees of freedom for complex physical systems, such as a synthetic frequency crystal. The concept of frequency synthetic dimension utilizes different optical frequency modes to form a lattice and induce coupling between lattice points through optical nonlinearities.[42,43] Leveraging the large bandwidth, good reconfigurability, and tunable gain/loss of photonic systems, frequency synthetic dimension is well suited to explore complicated systems that are difficult to implement or control in solid states, such as non-Hermitian,[44] high-dimensional,[45] and topological systems.[46] Here, we implement and perform *in situ* vector analysis of a synthetic frequency crystal on thin-film LN, which offers the desired low dissipation rate and strong nonlinear interaction via EO effect.[45,47,48] An LN racetrack resonator is employed to generate a set of frequency modes, separated by the FSR of the resonator (24.8 GHz). Efficient modulation, matching the FSR, is achieved through two pairs of electrodes with reversed polarity along the straight sections of the racetrack [Fig. 4(a)]. This creates strong EO coupling between adjacent frequency modes that emulates a tight-binding model[45] (more details are provided in Appendix F), where optical photons can hop between different lattice points with a large hopping rate proportional to the microwave driving voltage, which is also known as a resonant EO comb generator.[31] In the steady state of such an actively modulated resonator, input laser signals with different detuning effectively excite different Bloch states whose frequencies match the detuning [Fig. 4(b) (i) and (ii)]. Traditionally, probing only the optical transmission spectrum reveals the density-of-states of the frequency crystal.[45] Here, leveraging the *in situ* OVA system, we directly capture both the amplitude and phase responses of the Bloch states within the crystal. This direct measurement unveils the collective phase dynamics of the Bloch states [Fig. 4(b) (iii) and (iv)]. Specifically, for a given laser detuning, a coherent summation [Fig. 4(b) (iii) and (iv)] of the phase responses of the excited Bloch states [Fig. 4(b) (i)] is obtained. The reversed phase response between adjacent Bloch states inside the energy band leads to coherent cancellation [Fig. 4(b) (iii)] on the detected phase dynamics (except for the energy band edges), resulting in a near-flat in-band phase response curve with two sharp phase changes at the top and bottom of the band [Fig. 4(b) (iv)]. Our experimental results under varying microwave signal powers (0, 15, 18, and 20 dBm) agree well with the theory, as shown in Fig. 4(c). By slightly detuning the RF frequency from the resonator FSR (detuning ~85 MHz), we further transition the frequency crystal dynamics into a triple resonance state where only three neighboring modes are strongly coupled [Fig. 4(d)], illustrating the reconfigurability of the amplitude and phase dynamics of the crystal. Our *in situ* OVA system represents a stable and compact technology for directly probing active systems with ultrafast modulation, offering extra degrees of freedom for investigating various complex physical systems using frequency synthetic dimensions.

3 Discussion and Conclusion

In summary, we propose and experimentally implement a miniaturized and flexible OVA system for integrated photonic devices featuring 50 kHz measurement resolution and 16.2 THz measurement bandwidth on the LN platform. The ability to place various DUTs on the same chip as the SSB-based OVA enables *in situ* measurements of the amplitude and phase responses, leading to unambiguous and accurate characterization of the

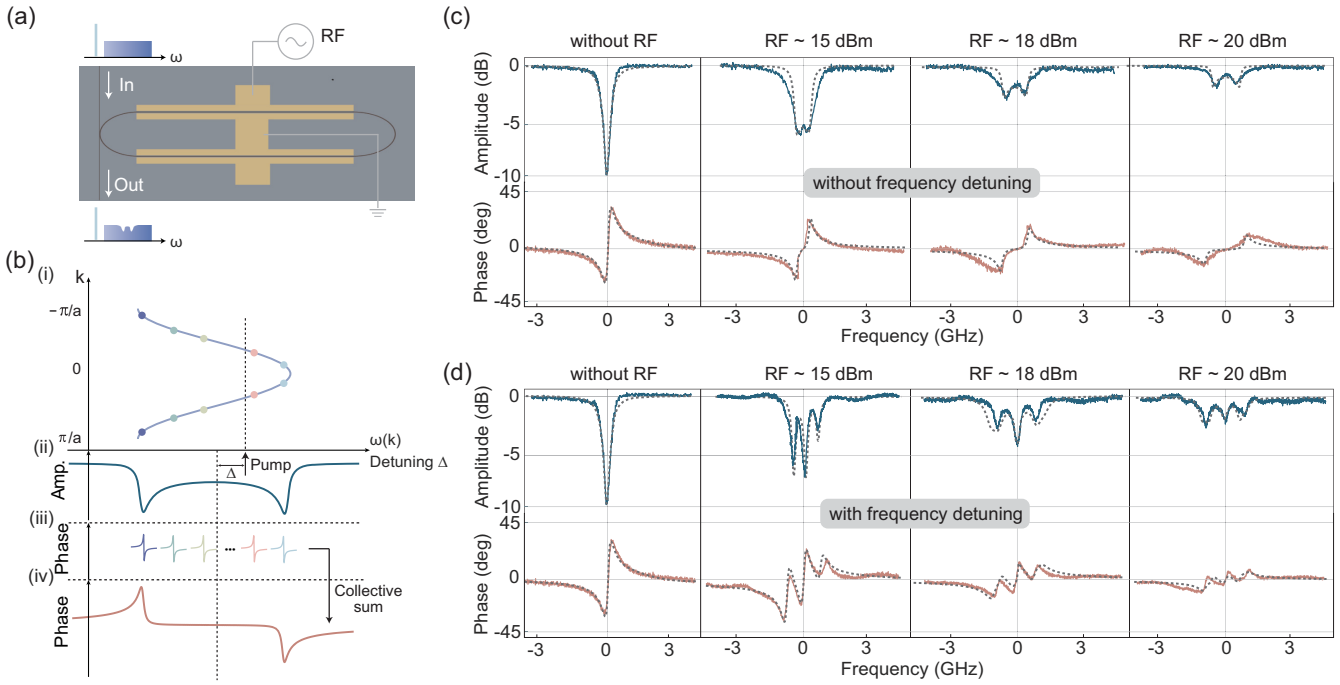

Fig. 4 *In situ* OVA for on-chip active devices. (a) Schematic illustration of *in situ* probing of an actively modulated microring resonator. Inset shows the microscope image of the LN resonant EO comb generator. (b), (i) Dispersion diagram of the synthetic frequency crystal, where different pump laser detunings excite Bloch modes with different energies and momenta. *a* is the lattice constant. (ii) Density of states of the frequency crystal as a function of laser detuning. (iii)–(iv) Coherent addition of the phase responses of individual Bloch modes (iii) leads to the measured collective phase dynamics of the Bloch states (iv). (c), (d) Measured (solid) and fitted (dashed) amplitude (blue) and phase (red) responses of the synthetic frequency crystal at increasing RF modulation power levels, without (c) and with (d) frequency detuning. Amp., amplitude.

intrinsic loss and coupling states of photonic devices. Moreover, we demonstrate the direct probing of full amplitude and phase dynamics of an actively modulated microresonator that emulates the Bloch states in the synthetic frequency dimension. This offers important extra degrees of freedom for understanding and investigating complex physical models like non-Hermitian, high-dimensional, and topological systems.

We envisage that the *in situ* OVA could become an important building block in future large-scale photonic networks that provide accurate and real-time monitoring and feedback control of on-chip elements. This could be achieved by combining the OVA with an electronic field programmable gate array (FPGA) chip, which can be trained to process the comprehensive spectral information extracted from the OVA and adjust the operation states of critical network components accordingly (see Note I in the Supplemental Material). The LN *in situ* OVA system could potentially also probe devices in other material platforms like Si or InP through hybrid packaging or heterogeneous integration. Moreover, our demonstrated system is highly compatible with other high-performance photonic components available on the integrated LN platform, such as frequency comb sources,[31,32,49] which could dramatically expedite the processing speed by parallel channelized measurement; and polarization-manipulation components,[50,51] which could be adopted to enable the retrieval of polarization dependent loss and polarization group delay. In addition, leveraging the wide transparency window of LN (from visible to mid-infrared),[20] the OVA system could be readily configured to function across a broad range of wavelengths that are of interest to not only optical communications and information technologies, but also biosensing, gas/nanoparticle detection, and atomic physics.

4 Appendix A: Design and Fabrication of the Devices

Devices are fabricated from a commercially available *x*-cut LNOI wafer (NANOLN), with a 500-nm LN thin film, a 4.7-μm buried SiO_2 layer, and a 500-μm silicon substrate. First, SiO_2 is deposited on the surface of a 4-in. LNOI wafer as an etching hard mask using plasma-enhanced chemical vapor deposition. Various functional devices are patterned on the entire wafer using an ASML UV Stepper lithography system (NFF, HKUST) die-by-die (1.5 cm × 1.5 cm) with a resolution of 500 nm. Next, the exposed resist patterns are transferred first to the SiO_2 layer using a standard fluorine-based dry etching process, and then to the LN device layer using an optimized Ar^+ based inductively coupled plasma reactive-ion etching process. The LN etch depth is ~250 nm, leaving a 250-nm-thick slab. After removal of the residual SiO_2 mask and redeposition, an annealing process is carried out. Afterward, second, third, and fourth lithography and lift-off processes are used to fabricate the microwave electrodes, heater, and wires/pads, respectively. Finally, chips are carefully cleaved for end-fire optical coupling with a total insertion loss of ~15 dB [including

10 dB coupling loss (5 dB/facet) and 4 dB on-chip loss (3 dB from the filter and 1 dB from the phase modulator)], and wire-bonded with a printed circuit board to realize multiport control of the TO phase shifters.

The 2×2 MMI is designed through full 3D finite-difference time-domain simulations (Ansys Lumerical) to serve as the resonator coupling region, providing the suitable imparted phase shift. The core MMI region has a size of 31.4 μm $\times$ 4.8 μm. The widths of the input waveguides are first tapered from 1.2 to 2.15 μm over a taper length of 15 μm before entering the MMI region to minimize scattering loss. The output waveguides are tapered in a similar but reversed manner.

5 Appendix B: Principle of RAMZI-Based Flat-Top Bandpass Filter

More details are presented here for the construction of the RAMZI filter. To achieve a "box-like" transfer function instead of the sinusoidal curve of a typical asymmetric MZI structure, the side-coupled ring resonator serves as a periodic phase shifter to adjust the transfer function. The FSR of the microring resonator determines the periodicity of these phase shifts, so the length relationship between the perimeter of the ring resonator and the length imbalance of MZI arms should satisfy $\Delta L_{\mathrm{mzi}} = \Delta L_{\mathrm{ring}}/2$, where ΔL_{mzi} is the length difference of the two MZI arms, and ΔL_{ring} is the perimeter of the ring resonator. When the propagation loss is negligible, the optical field of the RAMZI filter can be expressed as

$$E_{\mathrm{ramzi}} = \frac{1}{2}\left[E_{\mathrm{ring}} e^{-j(\phi_1+\phi_{\mathrm{ring}})} + 1 \cdot e^{-j\phi_2}\right], \tag{1}$$

where E_{ring} is the electric field amplitude of the ring resonator, ϕ_{ring} is the phase response of the ring resonator, and ϕ_1 and ϕ_2 are the phases induced in the two arms of the MZI. The output transfer function of the RAMZI filter can be written as

$$\begin{aligned} T_{\mathrm{ramzi}} &= |E_{\mathrm{ramzi}}|^2 \\ &= \frac{1}{4}\left[|E_{\mathrm{ring}}|^2 + 1 + 2|E_{\mathrm{ring}}| \cdot \cos(\phi_{\mathrm{ring}} - \phi_{\mathrm{mzi}})\right], \end{aligned} \tag{2}$$

where $\phi_{\mathrm{mzi}} = \phi_2 - \phi_1 = \beta \Delta L_{\mathrm{mzi}}$, β is the propagation constant, and ϕ_{ring} can be calculated as

$$\phi_{\mathrm{ring}} = \arctan \frac{(1-\kappa^2)\alpha \sin(\theta)}{(1+\alpha^2)\kappa - \alpha(1+\kappa^2)\cos(\theta)}, \tag{3}$$

where κ is the optical field coupling coefficient of the ring resonator, α is the amplitude attenuation coefficient of the ring resonator, and θ is the round-trip phase shift. In addition, the RAMZI configuration requires an external phase shift $\sim\pi/2$ between two branches of RAMZI to align the resonance notches with the quadrature point of the MZI. Therefore, the phase relation is expressed as $\beta \Delta L_{\mathrm{mzi}} = \frac{\beta \Delta L_{\mathrm{mzi}}}{2} \pm \frac{\pi}{2}$, and the following relation needs to be satisfied at the off-resonance points $[\theta = (2n+1)\cdot\pi, n = 1, 2, 3\ldots]$:

$$\frac{\mathrm{d}\phi_{\mathrm{ring}}}{\mathrm{d}\theta} = \frac{\mathrm{d}\phi_{\mathrm{mzi}}}{\mathrm{d}\theta}. \tag{4}$$

The calculated coupling coefficient of the ring resonator should be $\kappa = \frac{2\sqrt{2}}{3} \approx 0.94$. In this case, the phase response characteristics allow the RAMZI filter to flatten its bandpass region and sharpen the roll-off part.

6 Appendix C: Principle of SSB-Based OVA System

More details are presented here for the principle of the SSB-based OVA system. In the analysis of the operation for the SSB-based OVA system, the optical carrier is considered as $e^{jw_0 t}$, where ω_0 denotes the carrier frequency. The input RF signal is represented as $\cos \omega_{\mathrm{m}} t$, where ω_{m} is the scanning modulation frequency. The input electric field can be written as

$$\begin{aligned} E_{\mathrm{in}} &= e^{jw_0 t} e^{j\beta \cos \omega_{\mathrm{m}} t} \\ &\approx jJ_1(\beta) e^{j(\omega_0 - \omega_{\mathrm{m}})t} + J_0(\beta) e^{j\omega_0 t} + jJ_1(\beta) e^{j(\omega_0 + \omega_{\mathrm{m}})t}, \end{aligned} \tag{5}$$

where β is the modulation index and $J_n(\beta)$ $(n = 0, 1)$ is the Bessel function of the first kind. Considering small-signal modulation, the higher-order sidebands are ignored. After the Fourier transform, the input electric field can be written in the frequency domain as

$$\begin{aligned} E_{\mathrm{in}}(\omega) = {} & 2\pi j J_1(\beta)\delta(\omega - \omega_0 + \omega_{\mathrm{m}}) + 2\pi J_0(\beta)\delta(\omega - \omega_0) \\ & + 2\pi j J_1(\beta)\delta(\omega - \omega_0 - \omega_{\mathrm{m}}). \end{aligned} \tag{6}$$

When the signal passes through the flat-top bandpass filter, the optical carrier and one of the sidebands are preserved, resulting in SSB modulation. We assume the first term on the right-hand side of Eq. (6) is suppressed. When the remaining SSB signal is transmitted through the DUT, the output optical signal can be written as

$$\begin{aligned} E_{\mathrm{out}}(\omega) &= E_{\mathrm{in}}(\omega) H_{\mathrm{sys}}(\omega) H_{\mathrm{DUT}}(\omega) \\ &= 2\pi J_0(\beta)\delta(\omega - \omega_0) H_{\mathrm{sys}}(\omega_0) H_{\mathrm{DUT}}(\omega_0) \\ &\quad + 2\pi j J_1(\beta)\delta(\omega - \omega_0 - \omega_{\mathrm{m}}) H_{\mathrm{sys}}(\omega_0 + \omega_{\mathrm{m}}) H_{\mathrm{DUT}}(\omega_0 + \omega_{\mathrm{m}}), \end{aligned} \tag{7}$$

where $H_{\mathrm{sys}}(\omega)$ and $H_{\mathrm{DUT}}(\omega)$ are the transfer functions of the reference arm (used as OVA calibration background) and the DUT, respectively. After sending the signal to an AC-coupled PD, ignoring the DC and high-frequency terms, the output PD current could then be written as

$$\begin{aligned} i(\omega_{\mathrm{m}}) \propto {} & 4\pi^2 j R J_0(\beta) J_1(\beta) H^*_{\mathrm{sys}}(\omega_0) H^*_{\mathrm{DUT}}(\omega_0) H_{\mathrm{sys}}(\omega_0 + \omega_{\mathrm{m}}) \\ & \cdot H_{\mathrm{DUT}}(\omega_0 + \omega_{\mathrm{m}}), \end{aligned} \tag{8}$$

where R is the responsivity of the PD. The calibration process is performed by measuring the reference arm using the OVA system (without DUT). In this case, it is equivalent to $H_{\mathrm{DUT}}(\omega) = 1$, and the output current of the PD could then be written as

$$i_{\mathrm{sys}}(\omega_{\mathrm{m}}) = 4\pi^2 j R J_0(\beta) J_1(\beta) H^*_{\mathrm{sys}}(\omega_0) H_{\mathrm{sys}}(\omega_0 + \omega_{\mathrm{m}}). \tag{9}$$

Based on Eqs. (8) and (9), the spectral transfer function of the DUT can be obtained as

$$H(\omega_{\mathrm{m}}) = H_{\mathrm{DUT}}(\omega_0 + \omega_{\mathrm{m}}) = \frac{i(\omega_{\mathrm{m}})}{i_{\mathrm{sys}}(\omega_{\mathrm{m}}) H^*_{\mathrm{DUT}}(\omega_0)}. \tag{10}$$

In this equation, $H^*_{\mathrm{DUT}}(\omega_0)$ is the spectral response of the DUT at the optical carrier frequency, which can be considered as a complex constant. It is noted that Eq. (10) is only applicable in the absence of high-order sidebands, which could induce additional measurement errors at elevated input RF power levels (see Appendix G for more details).

7 Appendix D: Methodologies of the OVA Experiments

In our OVA experiment, the optical carrier from the tunable laser (Santec TSL-510) is sent to the LN chip using a lensed fiber after a polarization controller to ensure transverse electric (TE) polarization. The high-resolution scanning RF signals (10 to 50 GHz) are generated from a vector network analyzer (VNA, E5080B, 50 GHz) and loaded into the modulation electrodes via a high-speed probe (GGB Industries, 50 GHz). The output optical signals, which contain the full information of DUTs, are amplified using an EDFA (Amonics), detected by a high-speed photodetector (Finisar XPDV21X0RA, 50 GHz), and analyzed at another port of VNA. For ultrawide measurement experiments, two DC sources are utilized to shift the bandpass positions of filters to stitch different measurement channels.

8 Appendix E: Fitting of the Measured Device Parameters

In the fitting process for different on-chip devices, initial values and appropriate bounds are set for the parameters to be fitted, and the trust region algorithm is adopted to determine their optimal solution for the theory models. Specifically, for the single microring resonator, the key parameters, such as the coupling coefficient (κ), the resonator round-trip amplitude attenuation factor (a), and the perimeter of ring (L), are obtained. For the double ring system, building on the directional coupling theory,[53] the coupling coefficients of both rings (κ_1, κ_2), resonator round-trip amplitude attenuation factors (a_1, a_2), and the initial resonance frequency difference (Δf) between two rings can be obtained. For the CROW system, the time-domain coupling model[54] is adopted to fit the curve with the assumption of the identical coupling coefficient κ_{r} in the two ring–ring couplers, identical coupling coefficient κ_{b} in the two ring–bus couplers, as well as identical loss rates of the three rings. Then, the coupling coefficients $(\kappa_{\mathrm{r}}, \kappa_{\mathrm{b}})$, the resonator round-trip amplitude attenuation factor (a), and the perimeter (L) are retrieved.

9 Appendix F: Principle and Simulation of the Frequency Crystal Model

The Hamiltonian of the actively modulated microring resonator can be described as[45,47]

$$H = \sum_{j=-N}^{N} \omega_j a_j^{\dagger} a_j + \Omega \cos \omega_{\mathrm{m}} t (a_j^{\dagger} a_{j+1} + h.c.), \tag{11}$$

where ω_j is the frequency of each frequency mode, Ω is the coupling rate due to modulation, and ω_{m} is the frequency of the RF signal. The total number of frequency modes that are coupled is labeled by number $-N$ to N. Using the Heisenberg–Langevin equation, we obtain a set of equations of motion:

$$\dot{a}_j = \left(-i\omega_j - \frac{\kappa}{2}\right) a_j - i\Omega \cos \omega_{\mathrm{m}} t (a_{j+1} + a_{j-1}) - \sqrt{\kappa_{\mathrm{e}}} \alpha_{\mathrm{in}} e^{-i\omega_{\mathrm{L}} t} \delta_{j,0}. \tag{12}$$

Switching the system into the rotating frame by $a_j \to a_j e^{-i\omega_{\mathrm{L}} t} e^{-i\, j\omega_{\mathrm{m}} t}$ gives

$$\dot{a}_j = \left(i\Delta + il\delta - \frac{\kappa}{2}\right) a_j - i\frac{\Omega}{2} (a_{j+1} e^{i\phi} + a_{j-1} e^{-i\phi}) - \sqrt{\kappa_{\mathrm{e}}} \alpha_{\mathrm{in}} \delta_{j,0}. \tag{13}$$

We perform a transformation: $c_q = \frac{1}{\sqrt{N_t}} \sum_j a_j e^{-iqj}$ and $a_j = \frac{1}{\sqrt{N_t}} \sum_q c_q e^{iqj}$ with $N_t = 2N + 1$. In the case that $\delta = 0$ (note that, for the case of $\delta \neq 0$, it effectively couples fewer modes; therefore the phenomena can be simulated by reducing the N), we have

$$\dot{c_q} = \left(i\Delta - \frac{\kappa}{2}\right) c_q - i\Omega \cos(q + \phi) c_q - \sqrt{N_t \kappa_{\mathrm{e}}} \alpha_{\mathrm{in}}. \tag{14}$$

In the steady state, we can derive the expression of $c_q = \sqrt{\kappa_{\mathrm{e}} N_t} \alpha_{\mathrm{in}} \frac{1}{i\Delta - \frac{\kappa}{2} - i\Omega \cos(q+\phi)}$. The final output signal from the device can be written as $a_{\mathrm{out}} = (\alpha_{\mathrm{in}} + \sqrt{\kappa_{\mathrm{e}}} \sum_j a_j e^{-ij\omega_{\mathrm{m}} t}) = (\alpha_{\mathrm{in}} + \sqrt{\frac{\kappa_{\mathrm{e}}}{N_t}} c_{q=\omega t})$. The amplitude and phase responses can be extracted as $|a_{\mathrm{out}}|^2$ and $\mathrm{Arg}(a_{\mathrm{out}})$. The photodetector averages the a_{out} within a certain time; therefore the measured phase response is a collective sum of a_{out} over the excited modes c_q.

10 Appendix G: Errors from High-Order Sidebands and Noise

Error analysis in this work is performed by calculating the mean absolute error (MAE) between the simulation results and the ideal frequency responses (using a single microring resonator as an example) due to noise and higher-order sidebands, at different input RF power levels. As shown in Fig. 5, low measurement errors of <1% (dash line) could be maintained within the input RF powers of −10 to 15 dBm. The error on the low RF power side is mainly due to decreased signal-to-noise ratios (as shown in the left inset), whereas on the high RF power side is restricted by the existence of high-order sidebands (as shown in the right inset). During our real experiments, the input RF power is around 5 dBm (blue star in Fig. 5), where the noise and the high-order sidebands would not severely influence the results.

If the high input RF power is needed, this undesired error could also be effectively suppressed by conducting two consecutive measurements, i.e., one with the optical carrier and another without the optical carrier to obtain the subtracting results with higher accuracy.[52]

11 Appendix H: Performance Comparison with Previous OVA Systems

Table 1 lists a detailed performance comparison among various previously demonstrated OVA schemes, including MWP-based (SSB and DSB), interferometry-based, optical channel estimation-based, and laser-chirping-based methods. The performance metrics include the integration level, *in situ* measurement ability, resolution, measurement range, and dynamic range. As can be

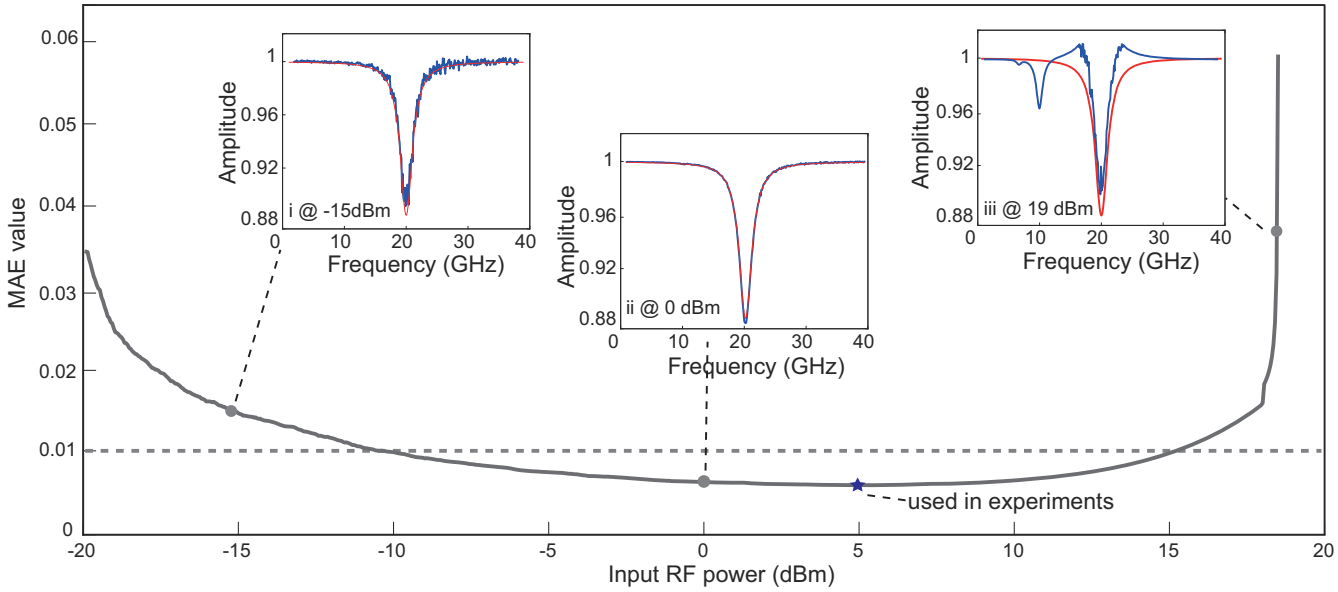

Fig. 5 Simulated MAE value as a function of the input RF power. Insets show the simulated amplitude results (blue) and the ideal ones (red) of a single microring resonator at −15 dBm (left), 0 dBm (middle), and 19 dBm (right).

Table 1 Performance comparison with various OVA schemes.

Working principle	Platform	*In situ* measurement	Resolution	Measurement range	Dynamic range	Ref.
SSB modulation	On-chip	Yes	50 kHz	16.2 THz	20 dB	This work
	Bulk	No	1.25 MHz	18 GHz	N/A	Ref. 6
	Bulk	No	78 kHz	40 GHz	20 dB	Ref. 8
	Bulk	No	25 MHz	80.05 GHz	N/A	Ref. 9
	Bulk	No	1 MHz	105 GHz	N/A	Ref. 10
	Bulk mod. + on-chip filter	No	23.4 kHz	70 GHz	23 dB	Ref. 14
	Bulk mod. + on-chip filter	No	150 MHz	18 GHz	29 dB	Ref. 15
Interferometry	Bulk	No	200 MHz	Several THz	60 dB	Ref. 2
Optical channel estimation	Bulk	No	0.732 MHz	250 GHz	N/A	Ref. 3
	Bulk	No	5.86 MHz	10 GHz	15 dB	Ref. 4
DSB modulation	Bulk	No	667 kHz	80 GHz	N/A	Ref. 11
	Bulk	No	10 MHz	40 GHz	N/A	Ref. 12
	Bulk	No	334 Hz	1.075 THz	90 dB	Ref. 13
Laser chirping	Bulk	No	471 kHz	55.1 THz	56 dB	Ref. 16

N/A, information not available or not applicable; mod., modulator.

seen, our work has demonstrated the first integrated OVA system with good overall performance and functionality. More specifically, OVA technologies based on MWP approaches (whether SSB or DSB) generally feature better resolutions than optical scanning schemes (interferometry or optical channel estimation). This is because MWP technology shifts the scanning frequency from the optical domain to the more precise RF domain, enabling theoretical resolutions as low as hertz level. Our current resolution is mainly limited by the linewidth of the laser (around 50 kHz), which can be further improved by adopting an ultranarrow linewidth laser.[13] In addition, our measurement range surpasses all reported SSB-based methods owing to the employment of a spectrum-stitching scheme. Although the measurement dynamic range is currently limited by the extinction ratio of the flat-top filter, this could potentially be improved by further optimizing the fabrication process and/or adoption of new filter configurations. We note that previous demonstrations based on DSB[13] and laser chirping[16] schemes show impressive and all-round performance metrics. Yet these systems are substantially more complicated, bulky, and costly (e.g., three modulators used in Ref. 13 and three lasers in Ref. 16) compared to our system.

Code and Data Availability

The data and code for numerical calculation that support the findings of this study are available from the corresponding author upon reasonable request.

Author Contributions

H.F. and C.W. conceived the idea. H.F. designed and fabricated the wafer with the help of Z.C., Y.Z., K.Z., and W.S. T.G. and Y.H. performed the numerical simulations. H.F., Z.W., and Y.Z. carried out the measurement and analyzed the data with the help of T.G. and Y.H., and H.F. prepared the manuscript with contributions from all authors. C.W. supervised the project.

Funding Information

This work was supported by the Research Grants Council, University Grants Committee (CityU 11212721, CityU 11204022, N_CityU113/20, C1002-22Y); and Croucher Foundation (9509005).

Disclosures

The authors declare no conflicts of interest.

Acknowledgments

We thank Prof. Marko Lončar for valuable support and Dr. Bitao Shen for fruitful discussions. We thank the technical support of Mr. Chun Fai Yeung, Mr. Shun Yee Lao, Mr. C. W. Lai, and Mr. Li Ho at HKUST, Nanosystem Fabrication Facility (NFF) for the stepper lithography and PECVD process. We thank Dr. Wing-Han Wong and Dr. Keeson Shum at City U for their help in measurement and device fabrication.

References

1. Z. Yang et al., "Miniaturization of optical spectrometers," *Science* **371**, eabe0722 (2021).
2. D. K. Gifford et al., "Optical vector network analyzer for single-scan measurements of loss, group delay, and polarization mode dispersion," *Appl. Opt.* **44**(34), 7282–7286 (2005).
3. C. Jin et al., "High-resolution optical spectrum characterization using optical channel estimation and spectrum stitching technique," *Opt. Lett.* **38**(13), 2314–2316 (2013).
4. X. Yi et al., "Characterization of passive optical components by DSP-based optical channel estimation," *IEEE Photonics Technol. Lett.* **24**(6), 443–445 (2011).
5. E. Voges et al., "Optical phase and amplitude measurement by single sideband homodyne detection," *IEEE J. Quantum Electron.* **18**(1), 124–129 (1982).
6. R. Hernández, A. Loayssa, and D. Benito, "Optical vector network analysis based on single-sideband modulation," *Opt. Eng.* **43**, 2418–2421 (2004).
7. S. Pan and M. Xue, "Ultrahigh-resolution optical vector analysis based on optical single-sideband modulation," *J. Lightwave Technol.* **35**(4), 836–845 (2016).
8. Z. Tang, S. Pan, and J. A. Yao, "A high resolution optical vector network analyzer based on a wideband and wavelength-tunable optical single-sideband modulator," *Opt. Express* **20**(6), 6555–6560 (2012).
9. W. Li et al., "Optical vector network analyzer based on single-sideband modulation and segmental measurement," *IEEE Photonics J.* **6**, 7901108 (2014).
10. M. Xue et al., "Wideband optical vector network analyzer based on optical single-sideband modulation and optical frequency comb," *Opt. Lett.* **38**(22), 4900–4902 (2013).
11. T. Qing et al., "Optical vector analysis based on asymmetrical optical double-sideband modulation using a dual-drive dual-parallel Mach-Zehnder modulator," *Opt. Express* **25**(5), 4665–4671 (2017).
12. T. Qing et al., "Measurement of optical magnitude response based on double-sideband modulation," *Opt. Lett.* **39**(21), 6174–6176 (2014).
13. T. Qing et al., "Optical vector analysis with attometer resolution, 90-dB dynamic range and THz bandwidth," *Nat. Commun.* **10**(1), 5135 (2019).
14. L. Li et al., "High-resolution optical vector network analyzer based on silicon-on-insulator coupled-resonator optical waveguides," in *ICECOM*, pp. 1–4 (2016).
15. S. X. Chew et al., "Silicon-on-insulator dual-ring notch filter for optical sideband suppression and spectral characterization," *J. Lightwave Technol.* **34**(20), 4705–4714 (2016).
16. Y.-H. Luo et al., "A wideband, high-resolution vector spectrum analyzer for integrated photonics," *Light: Sci. Appl.* **13**(1), 83 (2024).
17. D. Marpaung, J. Yao, and J. Capmany, "Integrated microwave photonics," *Nat. Photon.* **13**(2), 80–90 (2019).
18. J. Capmany and D. Novak, "Microwave photonics combines two worlds," *Nat. Photon.* **1**(6), 319–330 (2007).
19. H. Feng et al., "Integrated lithium niobate microwave photonic processing engine," *Nature* **627**(8002), 80–87 (2024).
20. D. Zhu et al., "Integrated photonics on thin-film lithium niobate," *Adv. Opt. Photon.* **13**(2), 242–352 (2021).
21. A. Boes et al., "Lithium niobate photonics: unlocking the electromagnetic spectrum," *Science* **379**, eabj4396 (2023).
22. C. Wang et al., "Integrated lithium niobate electro-optic modulators operating at CMOS-compatible voltages," *Nature* **562**(7725), 101–104 (2018).
23. M. He et al., "High-performance hybrid silicon and lithium niobate Mach–Zehnder modulators for 100 Gbit s^{-1} and beyond," *Nat. Photon.* **13**(5), 359–364 (2019).
24. H. Feng et al., "Ultra-high-linearity integrated lithium niobate electro-optic modulators," *Photonics Res.* **10**(10), 2366–2373 (2022).
25. M. Xu et al., "Dual-polarization thin-film lithium niobate in-phase quadrature modulators for terabit-per-second transmission," *Optica* **9**(1), 61–62 (2022).
26. P. Kharel et al., "Breaking voltage–bandwidth limits in integrated lithium niobate modulators using micro-structured electrodes," *Optica* **8**(3), 357–363 (2021).
27. M. Zhang et al., "Monolithic ultra-high-Q lithium niobate microring resonator," *Optica* **4**(12), 1536–1537 (2017).
28. W. Ke et al., "Digitally tunable optical delay line based on thin-film lithium niobate featuring high switching speed and low optical loss," *Photonics Res.* **10**(11), 2575–2583 (2022).
29. K. Abdelsalam et al., "Tunable dual-channel ultra-narrowband Bragg grating filter on thin-film lithium niobate," *Opt. Lett.* **46**(11), 2730–2733 (2021).
30. X. P. Li, K. X. Chen, and L. F. Wang, "Compact and electro-optic tunable interleaver in lithium niobate thin film," *Opt. Lett.* **43**(15), 3610–3613 (2018).
31. M. Zhang et al., "Broadband electro-optic frequency comb generation in a lithium niobate microring resonator," *Nature* **568**(7752), 373–377 (2019).
32. C. Wang et al., "Monolithic lithium niobate photonic circuits for Kerr frequency comb generation and modulation," *Nat. Commun.* **10**(1), 978 (2019).
33. K. Ye et al., "Surface acoustic wave stimulated Brillouin scattering in thin-film lithium niobate waveguides," arXiv:2311.14697 (2023).
34. C. C. Rodrigues et al., "On-chip backward stimulated Brillouin scattering in lithium niobate waveguides," arXiv:2311.18135 (2023).

35. S. Zhu et al., "Integrated lithium niobate photonic millimeter-wave radar," arXiv:2311.09857 (2023).
36. A. Rizzo et al., "Ultra-broadband interleaver for extreme wavelength scaling in silicon photonic links," *IEEE Photonics Technol. Lett.* **33**(1), 55–58 (2020).
37. H. Guan et al., "Passive silicon ring-assisted Mach–Zehnder interleavers operating in the broadband spectral range," *Appl. Opt.* **59**(27), 8349–8354 (2020).
38. J. Song et al., "Passive ring-assisted Mach-Zehnder interleaver on silicon-on-insulator," *Opt. Express* **16**(12), 8359–8365 (2008).
39. B. Peng et al., "What is and what is not electromagnetically induced transparency in whispering-gallery microcavities," *Nat. Commun.* **5**(1), 5082 (2014).
40. C. Wang et al., "Coherent perfect absorption at an exceptional point," *Science* **373**(6560), 1261–1265 (2021).
41. R. R. Kumar, X. Wu, and H. K. Tsang, "Compact high-extinction tunable CROW filters for integrated quantum photonic circuits," *Opt. Lett.* **45**(6), 1289–1292 (2020).
42. L. Yuan et al., "Synthetic dimension in photonics," *Optica* **5**(11), 1396–1405 (2018).
43. A. Dutt et al., "Creating boundaries along a synthetic frequency dimension," *Nat. Commun.* **13**(1), 3377 (2022).
44. K. Wang et al., "Topological complex-energy braiding of non-Hermitian bands," *Nature* **598**(7879), 59–64 (2021).
45. Y. Hu et al., "Realization of high-dimensional frequency crystals in electro-optic microcombs," *Optica* **7**(9), 1189–1194 (2020).
46. K. Wang et al., "Generating arbitrary topological windings of a non-Hermitian band," *Science* **371**(6535), 1240–1245 (2021).
47. Y. Hu et al., "Mirror-induced reflection in the frequency domain," *Nat. Commun.* **13**(1), 6293 (2022).
48. K. Zhang et al., "Spectral engineering of optical microresonators in anisotropic lithium niobate crystal," *Adv. Mater.* **36**, 2308840 (2024).
49. K. Zhang et al., "A power-efficient integrated lithium niobate electro-optic comb generator," *Commun. Phys.* **6**(1), 17 (2023).
50. Z. Chen et al., "Broadband adiabatic polarization rotator-splitter based on a lithium niobate on insulator platform," *Photonics Res.* **9**(12), 2319–2324 (2021).
51. Z. Lin et al., "High-performance polarization management devices based on thin-film lithium niobate," *Light: Sci. Appl.* **11**(1), 93 (2022).
52. M. Xue, S. Pan, and Y. Zhao, "Accuracy improvement of optical vector network analyzer based on single-sideband modulation," *Opt. Lett.* **39**(12), 3595–3598 (2014).
53. M. Tomita et al., "Tunable Fano interference effect in coupled-microsphere resonator-induced transparency," *J. Opt. Soc. Am. B* **26**(4), 813–818 (2009).
54. H. -C. Liu and A. Yariv, "Synthesis of high-order bandpass filters based on coupled-resonator optical waveguides (CROWs)," *Opt. Express* **19**(18), 17653–17668 (2011).

Hanke Feng received his PhD from City University of Hong Kong in 2024. He is currently a postdoctoral researcher at City University of Hong Kong. His research interests focus on integrated lithium niobate photonic circuits and system-level applications in microwave photonics and optical communications. He was recognized as a Rising Star of Microwave Photonics, China, in 2024.

Tong Ge is an undergraduate student at City University of Hong Kong. His research interests focus on integrated photonics, microwave photonics, and nonlinear optics. He is the recipient of the IET Prize 2022.

Yaowen Hu is an assistant professor at Peking University. He received his BS degree from Tsinghua University in 2018 and his PhD from Harvard University in 2023. His research focuses on quantum optics, nonlinear optics, photonic neuromorphic computing, and optical frequency combs. He was recognized in the *MIT Technology Review* 35 Innovators Under 35 (China) in 2023.

Zhenzheng Wang is a PhD student at City University of Hong Kong. He received his MS degree from Huazhong University of Science and Technology (2017). His research focuses on optical microcavities and packaging of lithium niobate photonics.

Yiwen Zhang is a PhD candidate at City University of Hong Kong. She received her BS degree from Shandong University in 2016 and her MS degree from Zhejiang University in 2019. Her research is focused on terahertz technologies on lithium niobate and their applications.

Zhaoxi Chen received his BS and MS degrees from Tianjin University and his PhD from City University of Hong Kong. He is currently a postdoctoral researcher in City University of Hong Kong. His recent research includes integrated lithium niobate photonics, especially in optical frequency comb.

Ke Zhang is a postdoctoral researcher at City University of Hong Kong and the CEO of Kokoxili Photonics Limited. He received his BS and MS degrees from the University of Science and Technology Beijing in 2014 and 2017, respectively, and his PhD from City University of Hong Kong in 2023. His work focuses on developing power-efficient chips in integrated lithium niobate platform.

Wenzhao Sun is an assistant professor at City University of Hong Kong (Dongguan). He received his BS, MS, and PhD degrees from Harbin Institute of Technology. His research focuses on micro & nanophotonics, microcavity, perovskite lasers, and integrated devices.

Cheng Wang is an associate professor at City University of Hong Kong. He received his BS degree from Tsinghua University in 2012 and his PhD from Harvard University in 2017. His research interests focus on integrated lithium niobate photonic and their applications in the fields of optical communication, microwave photonics, and nonlinear optics. He received the NSFC Excellent Young Scientist Fund in 2019 and the Croucher Innovation Award in 2020, and was recognized in the *MIT Technology Review* 35 Innovators Under 35 (China) in 2021.